

Microscopic description of quadrupole collectivity in neutron-rich nuclei across the N=126 shell closure

R. Rodríguez-Guzmán,^{1,*} L.M. Robledo,^{2,†} and M. M. Sharma^{1,‡}

¹*Physics Department, Kuwait University, Kuwait 13060*

²*Departamento de Física Teórica, Módulo 15, Universidad Autónoma de Madrid, 28049-Madrid, Spain*

(Dated: October 21, 2018)

The quadrupole collectivity in Nd, Sm, Gd, Dy, Er, Yb, Hf and W nuclei with neutron numbers $122 \leq N \leq 156$ is studied, both at the mean field level and beyond, using the Gogny energy density functional. Besides the robustness of the N=126 neutron shell closure, it is shown that the onset of static deformations in those isotopic chains with increasing neutron number leads to an enhanced stability and further extends the corresponding two-neutron driplines far beyond what could be expected from spherical calculations. Independence of the mean field predictions with respect to the particular version of the Gogny energy density functional employed is demonstrated by comparing results based on the D1S and D1M parameter sets. Correlations beyond mean field are taken into account in the framework of the angular momentum projected generator coordinate method calculation. It is shown that N=126 remains a robust neutron magic number when dynamical effects are included. The analysis of the collective wave functions, average deformations and excitation energies indicate that, with increasing neutron number, the zero-point quantum corrections lead to dominant prolate configurations in the 0_1^+ , 0_2^+ , 2_1^+ and 2_2^+ states of the studied nuclei. Moreover, those dynamical deformation effects provide an enhanced stability that further supports the mean field predictions, corroborating a shift of the r-process path to higher neutron numbers. Beyond mean field calculations provide a smaller shell gap at N=126 than the mean field one in good agreement with previous theoretical studies. However, the shell gap still remains strong enough in the two-neutron driplines.

PACS numbers: 24.75.+i, 25.85.Ca, 21.60.Jz, 27.90.+b, 21.10.Pc

I. INTRODUCTION

The evolution of the shell structure and the associated quadrupole collectivity with nucleon number is among the most prominent features in atomic nuclei. Its study has received renewed interest in recent years due to the progress in our understanding of neutron-rich nuclei far away from the valley of stability brought by the Radioactive Ion Beam (RIB) facilities set up all over the world. Shell effects in neutron-rich nuclei turn out to be quite challenging and, at least in some cases, they cannot be interpreted using the experience accumulated for stable systems [1]. A typical example is the weakening/erosion of the N=20 and N=28 magic numbers in light neutron-rich nuclei (see, for example, [2–27] and references therein).

In a mean field framework, the nucleus ^{32}Mg is predicted to have a spherical ground state [11–13, 16–18]. However, the experimental $B(E2, 0_1^+ \rightarrow 2_1^+)$ value [4], the excitation energy of the 2_1^+ state [5, 6] as well as the ratio $E_{4_1^+}/E_{2_1^+}=2.6$ are all consistent with those of a deformed ground state. Within the Shell Model, the increased quadrupole collectivity in nuclei of this region has been explained by invoking neutron excitations across the

N=20 shell gap [9, 10]. On the other hand, it has been shown that effects not explicitly taken into account at the mean field level like the restoration of broken symmetries and configuration mixing, can account for a deformed ground state in ^{32}Mg and ^{30}Ne as well as the main physical trends in nuclei around the *island of inversion* [11–15]. This has been further corroborated by the recent study of the quadrupole collectivity in $^{28,30}\text{Ne}$ and $^{34,36}\text{Mg}$ [2]. The situation is slightly different in the case of neutron-rich nuclei around N=28 where Shell Model [19], mean field [11, 20–23] and beyond mean field [11, 15, 20] calculations predict deformed ground states, in agreement with experimental results [24–27], and indicating that this neutron shell closure is more fragile than the N=20 one.

The previous examples already illustrate the challenges encountered in the theoretical description of neutron-rich nuclei. They suggest that caution must be taken when invoking the weakening/erosion of neutron magic numbers and reveal that plain mean field approximations [28], while valuable as a starting point, may not be sufficient since the quadrupole properties in the considered nuclei may actually be determined by the subtle interplay between quantum corrections stemming from the restoration of the broken symmetries (mainly the rotational one) and fluctuations in the collective degrees of freedom. Similar conclusions can be extracted from other beyond mean field calculations (see, for example, [29–31] and references therein). On the neutron deficient side, symmetry-projected configuration mixing results in-

*Electronic address: raynerrobertorodriguez@gmail.com

†Electronic address: luis.robledo@uam.es

‡Electronic address: madan.sharma@ku.edu.kw

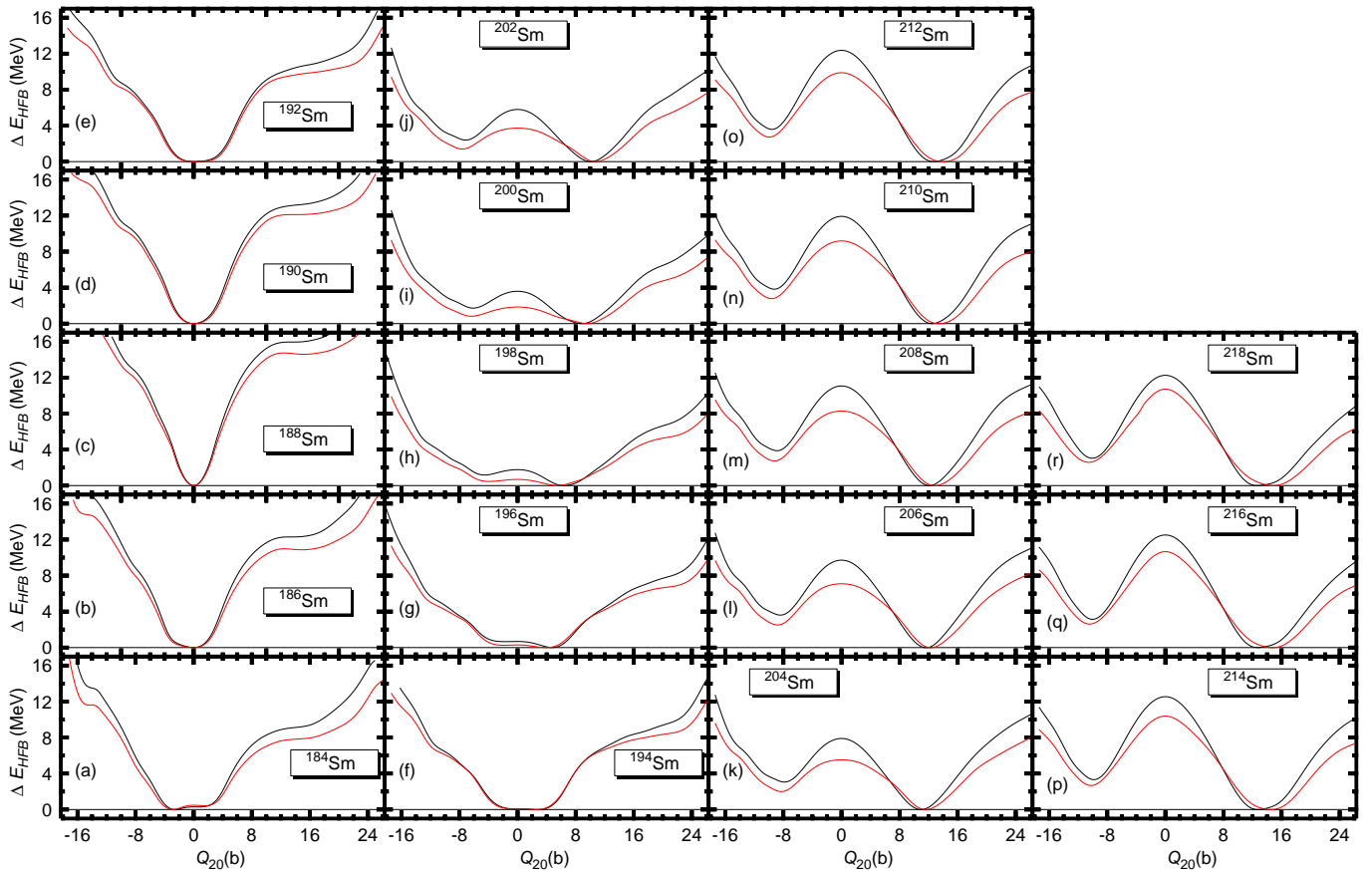


FIG. 1: (Color online) In panels (a)-(r) the MFPECs obtained for the $^{184-218}\text{Sm}$ isotopes with the Gogny-D1M (black) and Gogny-D1S (red) EDFs are depicted. Each curve is referred to its absolute minimum. Calculations have been carried out with $M_{z,Max}=14$. For more details, see the main text.

indicate that $Z=82$ remains, on the average, as a conserved magic proton number for Pb isotopes and support the experimental evidences for rotational bands built on co-existing low-lying prolate and oblate 0^+ states [32–34].

Shell effects play a crucial role in understanding the nucleosynthesis of nuclei heavier than Fe via the r-process [35–38]. Though different r-process scenarios and uncertainties are still under debate (see, for example, [39]), it is commonly accepted that the r-process passes through the neutron numbers $N=50$, 82 and 126 and that the synthesis of nuclei around them is revealed in the peaks of the r-process abundances around the mass numbers $A \approx 80$, 130 and 190, respectively. Therefore, a sound theoretical description of the shell effects around $N=50$, 82 and 126 represents a major goal not only for nuclear structure physics but also for astrophysics.

It should be kept in mind that, due to their large neutron excess, very neutron-rich nuclei near the r-process path remain out of reach experimentally, especially those in the heavy mass region. Therefore, our understanding of those systems requires the use of different theoretical tools whose predictions have been the subject of intense debate [40–44]. For example, shell quenching has been invoked [45, 46] at $N=82$ near the r-process path to

improve the predicted r-process abundances around the second peak. The anomalous behavior of the 2^+_1 states in neutron-rich Cd isotopes has even been cited [47] as an evidence for such a quenching. However, it has also been shown that this anomalous behavior can be naturally explained in the framework of symmetry-projected configuration mixing calculations [48] without the need to assume any quenching of the $N=82$ shell closure. This is further corroborated by experimental results on energy levels in ^{130}Cd [49, 50].

In the present work, we have studied the quadrupole collectivity in the region of the third peak of the r-process. To this end, we have considered even-even Nd, Sm, Gd, Dy, Er, Yb, Hf and W nuclei with neutron numbers $122 \leq N \leq 156$ extending beyond the two-neutron dripline. The constrained Hartree-Fock-Bogoliubov (HFB) approximation [28] is used to obtain the mean field potential energy curves (MFPECs) corresponding to the HFB energies as a function of the quadrupole moment. The MFPECs offer a valuable starting point to understand the evolution of the shell structure across $N=126$ as well as the emergence of quadrupole deformations in the considered isotopic chains. In particular, it will be shown that the onset

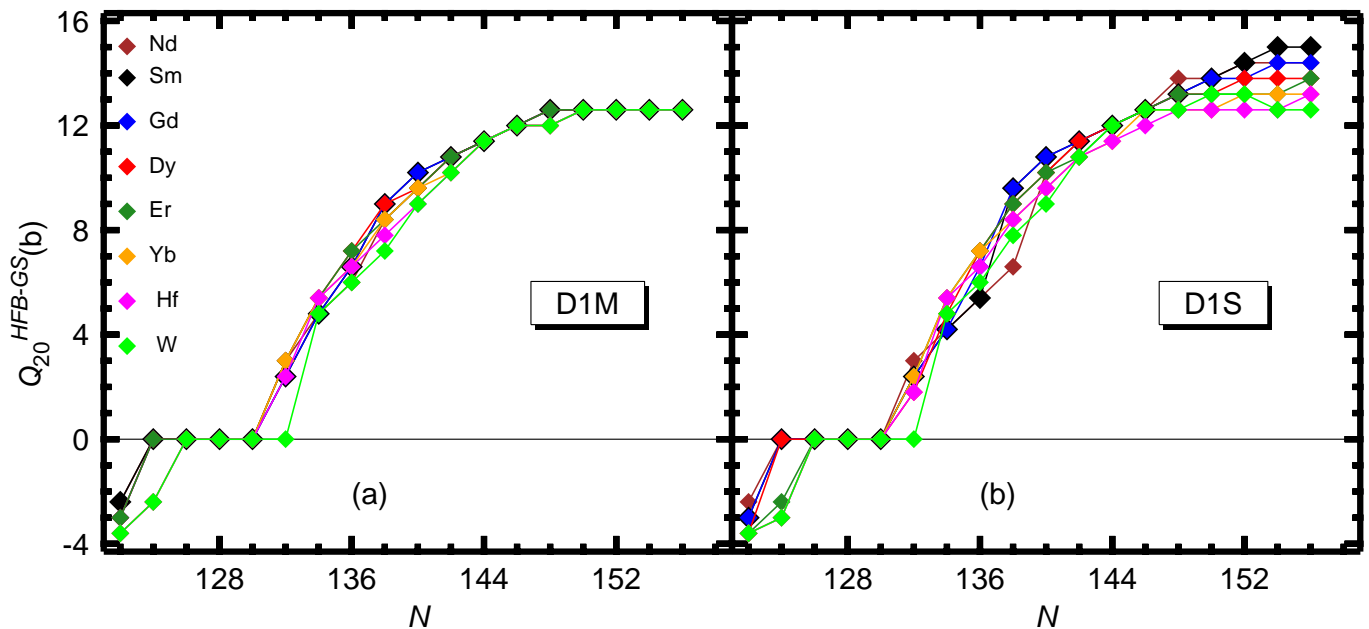


FIG. 2: (Color online) The ground state quadrupole deformations Q_{20}^{HFB-GS} obtained for the nuclei $^{182-216}\text{Nd}$, $^{184-218}\text{Sm}$, $^{186-220}\text{Gd}$, $^{188-222}\text{Dy}$, $^{190-224}\text{Er}$, $^{192-226}\text{Yb}$, $^{194-228}\text{Hf}$ and $^{196-230}\text{W}$ are plotted as a function of neutron number. Results are shown for the Gogny-D1M [panel (a)] and Gogny-D1S [panel (b)] EDFs. Calculations have been carried out with $M_{z,Max}=14$. For more details, see the main text.

of mean field (i.e., static) quadrupole deformation after crossing the spherical $N=126$ neutron shell closure leads to a pronounced enhancement of the two-neutron separation energies as compared with the ones resulting from the spherical HFB scheme.

The D1M parametrization [51] of the Gogny [52] EDF is used in all the HFB calculations. In some instances, however, results obtained with the Gogny-D1S [53] EDF will be shown for comparison. The reason is that the Gogny-D1S EDF has a strong reputation of being able to reproduce a large collection of low-energy nuclear data all over the nuclear chart both at the mean field level and beyond and related to deformation effects (see, for example, [11, 53–59] and references therein). However, it has to be kept in mind that D1S is not specially good in reproducing binding energies as shown in large scale calculations [60, 61] where a systematic drift is observed in the differences between the experimental and theoretical binding energies in heavy isotopes.

The D1M fitting protocol includes [51] both realistic neutron matter equation of state (EoS) information and the binding energies of all known nuclei. With an impressive rms of 0.798 MeV it represents a competitive choice to deal with nuclear masses. In addition to previous studies [51, 55, 56], new ones including fission properties in heavy and superheavy nuclei [62, 63] as well as odd nuclei within the equal filling approximation (EFA) [64–66], suggest that the Gogny-D1M EDF essentially retains the predictive power of the well tested D1S parametrization and therefore it represents a good candidate to replace the latter.

The MFPECs obtained within the Gogny-HFB framework display, at least for some Nd, Sm, Gd, Dy, Er, Yb, Hf and W nuclei, competing minima based on different intrinsic configurations indicating that beyond mean field correlations like symmetry restoration and/or quadrupole configuration mixing, may play a role. That the restoration of the broken rotational symmetry may provide leading quantum corrections can be expected from the fact that the energy gain associated with it (i.e., the so called rotational correction) is proportional to the deformation of the intrinsic HFB states [12, 67]. Similar to what has been found in other regions of the nuclear chart [11–13, 20], symmetry restoration also leads in some of the studied nuclei to important topological changes in the angular momentum projected potential energy curves (AMPPECs) as compared with the corresponding MFPECs. Therefore, it is also important to consider the effect of the quadrupole configuration mixing in those cases. Moreover, even in those nuclei where the AMPPECs exhibit well defined minima, it is important to check their stability with respect to quadrupole fluctuations since not only the energy landscape but also the underlying collective inertia play a role within a dynamical treatment. With this in mind we have performed angular momentum projected generator coordinate method (AMPGCM) calculations [11], based on the Gogny-D1M EDF, for all the nuclei studied in this work. In addition to the spectroscopic properties of the excited state the AMPGCM also provides the ground state correlation energy that, as we will see, plays an important role in the properties of the $N=126$ shell closure.

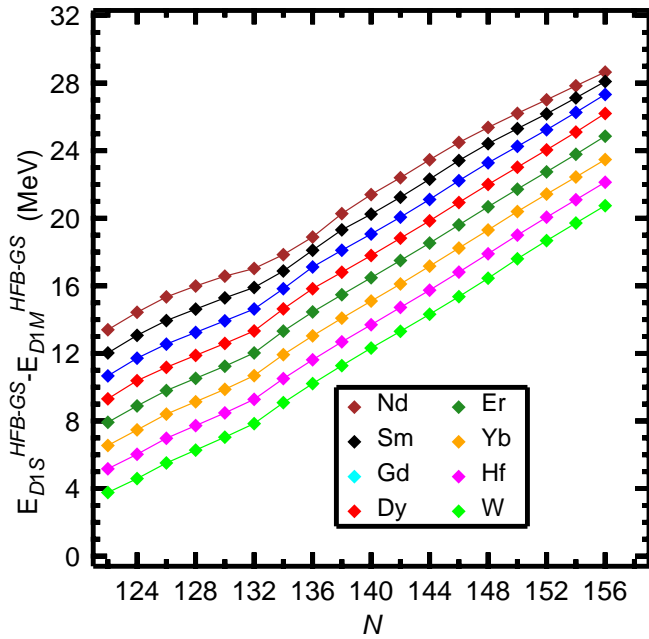


FIG. 3: (Color online) The differences $E_{D1S}^{HFB-GS} - E_{D1M}^{HFB-GS}$ between the HFB ground state energies obtained for the nuclei $^{182-216}\text{Nd}$, $^{184-218}\text{Sm}$, $^{186-220}\text{Gd}$, $^{188-222}\text{Dy}$, $^{190-224}\text{Er}$, $^{192-226}\text{Yb}$, $^{194-228}\text{Hf}$ and $^{196-230}\text{W}$ with the D1M and D1S parametrizations are plotted as a function of neutron number.

The paper is organized as follows. In Sec. II, we describe the theoretical approximations used. The key ingredients of our HFB approach are presented in Sec. II A while the AMPGCM formalism [11] is briefly outlined in Sec. II B. The results of the calculations are discussed in Sec. III. First, in Sec. III A, we discuss the static quadrupole properties predicted within our HFB calculations. The results of our symmetry-projected configuration mixing study are presented in Sec. III B. Finally, Sec. IV is devoted to the concluding remarks and work perspectives.

II. THEORETICAL FRAMEWORK

In this section, the theoretical approximations used in the present work are described. First, in Sec. II A, the HFB framework [28] is introduced. Next the AMPGCM formalism [11] is briefly outlined in Sec. II B. For a more detailed description of both angular momentum projection (AMP) and the Generator Coordinate Method (GCM) the reader is referred to the literature [12, 68–72].

A. The Hartree-Fock-Bogoliubov approximation

The starting point is the (constrained) HFB approximation [28, 54] for the finite range and density dependent Gogny-EDF [52]. Both the D1S [53] and D1M [51]

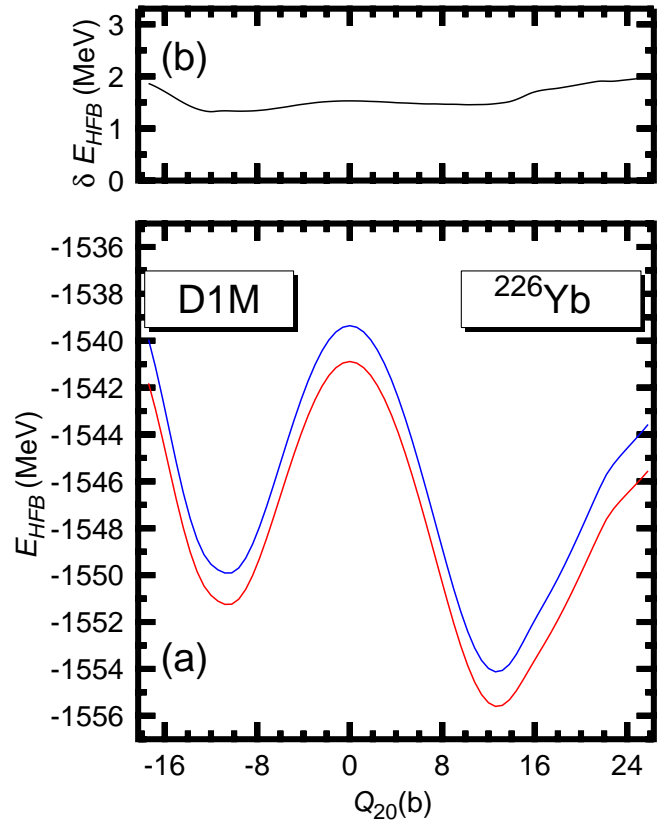


FIG. 4: (Color online) In panel (a) the HFB energies computed with $b_0=2.1$ fm and $M_{z,Max}=14$ (blue) and $M_{z,Max}=17$ (red) are plotted as a function of the quadrupole moment. Results are shown for the nucleus ^{226}Yb using the D1M parametrization. In panel (b), the energy difference between the $M_{z,Max}=14$ and $M_{z,Max}=17$ calculations is plotted as a function of the quadrupole moment.

parametrizations are considered. As constraining operators the axially symmetric quadrupole $\hat{Q}_{20} = z^2 - \frac{1}{2}(x^2 + y^2)$ [55, 56] moment as well as the standard HFB constraints on both the proton \hat{Z} and neutron \hat{N} number operators are used. The HFB quasiparticle operators are expanded in an axially symmetric and parity-preserving harmonic oscillator (HO) basis whose quantum numbers are restricted by the condition

$$2n_{\perp} + |m| + \frac{1}{q}n_z \leq M_{z,Max} \quad (1)$$

All the mean field results to be discussed later on have been obtained with $q=1.0$. The two length parameters b_z and $b_{\perp} = b_0$ characterizing the HO basis are chosen to be equal to keep the basis closed under rotations [11, 73] (this is also the reason to include full HO major shells in the basis). This simplifies the application of the AMPGCM approximation described in the next Sec. II B. Most of our results have been obtained with $M_{z,Max}=14$. However, we have also tested the stability of our predictions with respect to the size of the consid-

ered single-particle basis by performing HFB calculations with $M_{z,Max}=17$.

It should be kept in mind that for very neutron-rich nuclei, especially those in the proximity of the two-neutron dripline, the HFB approximation must be used [74, 75] and absolute convergence for the binding energy can only be obtained for HO bases with a very large number of shells $M_{z,Max}$. At the HFB level such a computationally demanding task can be afforded with present day computer capabilities. Also in the case that we were just interested in a single Q_{20} -configuration, AMP calculations with a very large $M_{z,Max}$ value could be afforded. However, the considerable amount of angular momentum projected Hamiltonian kernels to be computed in the AMPGCM calculations (see, Sec. II B), restrict the maximum $M_{z,Max}$ value to $M_{z,Max} = 14$. The reason behind is the finite range component of the Gogny-EDF that makes the evaluation of the corresponding matrix elements very time consuming. On the other hand, as the collective motion is mainly affected by the shape of the energy landscape, not its absolute depth, a quicker convergence with $M_{z,Max}$ is achieved for the related physical quantities.

The HFB equations have been solved with the help of an approximate second order gradient method [76] which allows us to handle constraints efficiently [55, 56, 62, 63, 77]. The method is based on the parametrization of a given HFB vacuum in terms of the Thouless theorem [28]. Recently, similar variational strategies have been applied to correlated electronic systems in condensed matter physics [78, 79] and quantum chemistry [80, 81].

The constrained HFB approximation provides us with a set of mean field product states $|\varphi(Q_{20})\rangle$, labeled by the generating coordinate $\langle\varphi|\hat{Q}_{20}|\varphi\rangle = Q_{20}$, as well as the MFPECs. In our calculations we have used the grid $-26 \text{ b} \leq Q_{20} \leq 36 \text{ b}$ with a mesh size $\delta Q_{20} = 0.6 \text{ b}$. We have tested that they are accurate enough to describe the low-energy quadrupole dynamics of the nuclei considered. In particular, as will be shown, the selected Q_{20} -grid is enough for the AMPGCM collective wave functions to reach the zero value in their tails (see, Sec.III B).

Other interesting pieces of information coming from the mean field approximation are the proton and neutron single-particle energies (SPEs). The quadrupole deformation effects are strongly linked to the position of the Fermi energies in such spectra [56, 82–84]. We have studied the evolution of the proton and neutron SPEs with the quadrupole moment Q_{20} . To this end, we have diagonalized the Routhian $h = t + \Gamma - \lambda_{Q_{20}} Q_{20}$, with t being the kinetic energy operator and Γ the Hartree-Fock field [28]. The term $\lambda_{Q_{20}} Q_{20}$ contains the Lagrange multiplier used to enforce the corresponding quadrupole constraint.

B. Symmetry-projected quadrupole configuration mixing

Having a set of symmetry breaking (i.e., intrinsic) HFB states $|\varphi(Q_{20})\rangle$ at hand, one introduces the following AMPGCM ansatz

$$|\Psi_{M,\sigma}^I\rangle = \sum_K \int dQ_{20} f_{K;\sigma}^I(Q_{20}) \hat{P}_{MK}^I |\varphi(Q_{20})\rangle \quad (2)$$

which superposes the symmetry-projected states $\hat{P}_{MK}^I |\varphi(Q_{20})\rangle$ with amplitudes $f_{K;\sigma}^I(Q_{20})$. The projection operator reads [28]

$$\hat{P}_{MK}^I = \frac{2I+1}{8\pi^2} \int d\Omega \mathcal{D}_{MK}^{I*} \hat{R}(\Omega) \quad (3)$$

where $R(\Omega) = e^{-i\alpha\hat{J}_z} e^{-i\beta\hat{J}_y} e^{-i\gamma\hat{J}_z}$ is the rotation operator, $\Omega = (\alpha, \beta, \gamma)$ stands for the set of Euler angles and $\mathcal{D}_{MK}^I(\Omega)$ are Wigner functions [85]. Our set of generating states $|\varphi(Q_{20})\rangle$ only comprises axially symmetric and parity-preserving $K=0$ HFB vacua (quasiparticle excitations [72] are not included). As a result, the integrals over α and γ can be carried out analytically and one is only left with the numerical β -integration over a suitable grid. The amplitudes $f_{K=0;\sigma}^I(Q_{20}) = f_{\sigma}^I(Q_{20})$ are then determined through the solution of the Hill-Wheeler (HW) equation [11, 86]

$$\int dQ'_{20} [\mathcal{H}^I(Q_{20}, Q'_{20}) - E_{\sigma}^I \mathcal{N}^I(Q_{20}, Q'_{20})] f_{\sigma}^I(Q'_{20}) = 0 \quad (4)$$

where

$$\begin{aligned} \mathcal{H}^I(Q_{20}, Q'_{20}) &= \Delta(I) (2I+1) \int_0^{\pi/2} d\beta \sin(\beta) h(\beta) \\ \mathcal{N}^I(Q_{20}, Q'_{20}) &= \Delta(I) (2I+1) \int_0^{\pi/2} d\beta \sin(\beta) n(\beta) \\ \Delta(I) &= \frac{1}{2} (1 + (-)^I) \\ h(\beta) &= \langle\varphi(Q_{20})|\hat{H}[\rho_{\beta}^{Mix}(\vec{r})]e^{-i\beta\hat{J}_y}|\varphi(Q'_{20})\rangle \\ n(\beta) &= \langle\varphi(Q_{20})|e^{-i\beta\hat{J}_y}|\varphi(Q'_{20})\rangle \end{aligned} \quad (5)$$

and $\rho_{\beta}^{Mix}(\vec{r})$ is the so-called *mixed density* prescription, i.e.,

$$\rho_{\beta}^{Mix}(\vec{r}) = \frac{\langle\varphi(Q_{20})|\hat{\rho}(\vec{r})e^{-i\beta\hat{J}_y}|\varphi(Q'_{20})\rangle}{\langle\varphi(Q_{20})|e^{-i\beta\hat{J}_y}|\varphi(Q'_{20})\rangle} \quad (6)$$

widely used in the context of symmetry restoration and/or configuration mixing [11, 32, 33, 55, 68, 87–89]. Since the average values of the proton and neutron numbers usually differ from the nucleus' proton Z_0 and neutron N_0 numbers we have replaced \hat{H} by

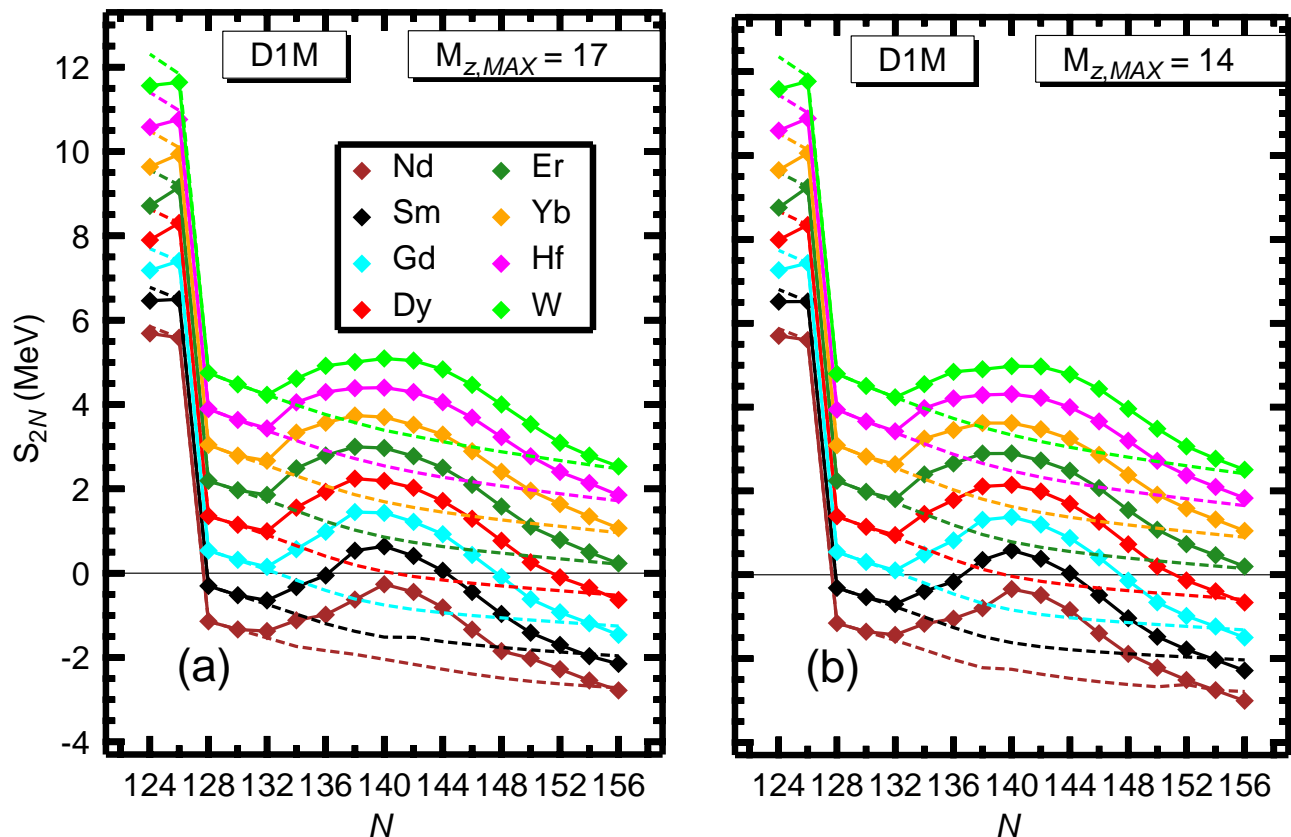


FIG. 5: (Color online) The two-neutron separation energies (full lines) computed within the HFB approximation for the nuclei $^{182-216}\text{Nd}$, $^{184-218}\text{Sm}$, $^{186-220}\text{Gd}$, $^{188-222}\text{Dy}$, $^{190-224}\text{Er}$, $^{192-226}\text{Yb}$, $^{194-228}\text{Hf}$ and $^{196-230}\text{W}$ are plotted as a function of the neutron number. Results based on the Gogny-D1M EDF and the bases $M_{z,MAX}=17$ and $M_{z,MAX}=14$ are shown in panels (a) and (b), respectively. The two-neutron separation energies obtained in the framework of spherical HFB calculations are also included in the plots (dashed lines) for comparison. For more details, see the main text.

$\hat{H} - \lambda_Z (\hat{Z} - Z_0) - \lambda_N (\hat{N} - N_0)$, where λ_Z and λ_N are chemical potentials for protons and neutrons, respectively [68, 71, 90]. All the AMPGCM calculations discussed in this work have been performed with the Gogny-D1M EDF and $M_{z,MAX}=14$.

For a given spin I , the solution of the HW equation (4) provides the energies E_σ^I corresponding to the ground ($\sigma=1$) and excited ($\sigma=2,3 \dots$) states. However, since the symmetry-projected basis states used in the expansion Eq.(2) are not orthogonal, the functions $f_\sigma^I(Q_{20})$ cannot be interpreted as probability amplitudes. One then introduces [11, 55] the collective wave functions

$$G_\sigma^I(Q_{20}) = \int dQ'_{20} \mathcal{N}^{I\frac{1}{2}}(Q_{20}, Q'_{20}) f_\sigma^I(Q'_{20}) \quad (7)$$

in terms of the operational square root of the norm kernel [11, 28]. The collective wave functions Eq. (7) are orthogonal and their modulus squared $|G_\sigma^I(Q_{20})|^2$ has the meaning of a probability amplitude [28]. In order to understand these collective wave functions in a more quantitative way, we have computed the averages [11]

$$Q_{20}^{I,\sigma} = \int dQ_{20} |G_\sigma^I(Q_{20})|^2 Q_{20} \quad (8)$$

providing us with a measure of the deformation in the underlying intrinsic states.

III. DISCUSSION OF RESULTS

In this section, the results of our calculations are discussed. First, in Sec. III A, the static quadrupole properties obtained within our Gogny-HFB framework are addressed. The results of the AMPGCM calculations with Gogny-D1M are presented in Sec. III B.

A. The HFB approximation: static quadrupole properties

In Fig. 1, we have plotted [panels (a)-(r)] a typical outcome of the constrained HFB calculations based on the Gogny D1M and D1S EDFs. The MFPECs are shown

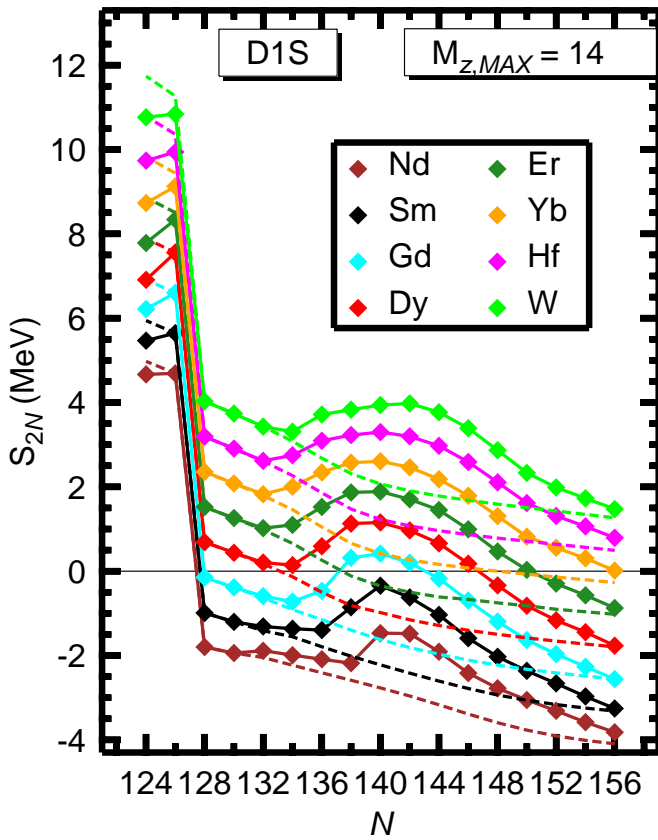


FIG. 6: (Color online) The two-neutron separation energies (full lines) computed within the Gogny-D1S HFB approximation for the nuclei $^{182-216}\text{Nd}$, $^{184-218}\text{Sm}$, $^{186-220}\text{Gd}$, $^{188-222}\text{Dy}$, $^{190-224}\text{Er}$, $^{192-226}\text{Yb}$, $^{194-228}\text{Hf}$ and $^{196-230}\text{W}$ are plotted as a function of neutron number. Results have been obtained with $M_{z,MAX}=14$. The two-neutron separation energies obtained in the framework of spherical HFB calculations are also included in the plots (dashed lines) for comparison.

for the nuclei $^{184-218}\text{Sm}$ taken as illustrative examples. For the sake of clarity they are depicted for $-18.3 \text{ b} \leq Q_{20} \leq 26.3 \text{ b}$. The HFB energies are always referred to the absolute minimum of the corresponding MFPEC. Calculations have been carried out with $M_{z,MAX}=14$.

It is apparent from the figure that, though the energies ΔE_{HFB} tend to be smaller with the parametrization D1S, both Gogny-EDFs provide MFPECs with a similar structure. The nucleus ^{184}Sm displays a slightly oblate ground state ($Q_{20}^{HFB-GS} = -2.4 \text{ b}$ and $Q_{20}^{HFB-GS} = -3.0 \text{ b}$ with the D1M and D1S parametrizations, respectively) while spherical ground states are predicted for $^{186-192}\text{Sm}$. In the case of ^{188}Sm , the MFPEC exhibits the clear signature of a strong $N=126$ neutron shell closure with vanishing neutron pairing energy at $Q_{20}=0$. Already for the isotope ^{194}Sm (i.e., $N=132$), the HFB ground state becomes slightly prolate deformed with $Q_{20}^{HFB-GS} = 2.4 \text{ b}$. Prolate deformed ground states are also predicted for the heavier isotopes $^{196-218}\text{Sm}$. Typical β_2 values for this chain are $\beta_2 = -0.07$ for ^{184}Sm , $\beta_2 = 0.06$ for ^{194}Sm and

$\beta_2 = 0.28$ for ^{214}Sm , all of them with the parametrization D1M. Similar results are found for the nuclei $^{182-216}\text{Nd}$, $^{186-220}\text{Gd}$, $^{188-222}\text{Dy}$, $^{190-224}\text{Er}$, $^{192-226}\text{Yb}$, $^{194-228}\text{Hf}$ and $^{196-230}\text{W}$ as can be seen from Fig. 2 where the ground state deformations Q_{20}^{HFB-GS} have been plotted as a function of neutron number for the Gogny-D1M [panel (a)] and Gogny-D1S [panel (b)] EDFs.

Therefore, in the framework of the Gogny-HFB calculations, $N=126$ appears as a spherical neutron magic number. However, 6-8 mass units beyond $N=126$, regardless of the Gogny-EDF employed, there is an onset of prolate deformation in the ground states along all the studied isotopic chains.

This effect agrees well with the additional stability beyond $N=126$ predicted in the relativistic mean field theory (RMF) based on the NL-SV1 Lagrangian model with the inclusion of the vector self-coupling of ω -meson [91–93]. A similar effect can also be seen in the mass formulas HFB-14 based upon Skyrme-HFB [94] and in the finite-range droplet model (FRDM) [95].

From Figs. 1 and 2 we conclude that both the D1M and D1S parametrizations provide quite similar deformation effects for the considered nuclei. However, the D1S results show a pronounced under-binding as can be seen in Fig. 3 where the ground state energy differences $E_{D1S}^{HFB-GS} - E_{D1M}^{HFB-GS}$ are plotted as a function of neutron number. This quantity increases almost linearly with neutron number while it decreases for increasing Z values. These results are not surprising as they reflect a well known deficiency [60] of the Gogny-D1S EDF away from the stability valley. A pronounced under-binding has also been found in the Gogny-D1S fission paths, as compared with the D1M ones, obtained in our recent studies of neutron-rich U and Pu nuclei as well as in superheavy elements [62, 63]. The linear increase of the D1S under-binding with neutron number implies that the behavior of the two-neutron separation energies will be similar to that with D1M but the quantity will be shifted down by roughly 1 MeV.

A few words concerning the convergence of our calculations are in order here. In panel (a) of Fig. 4, we have plotted the HFB energies, computed with $M_{z,MAX}=14$ and $M_{z,MAX}=17$, as a function of the quadrupole moment. In panel (b), we have plotted the energy difference between both calculations. Results are shown for ^{226}Yb and the Gogny-D1M EDF but similar ones are obtained for other nuclei and/or the D1S parametrization. In the range $-18.3 \text{ b} \leq Q_{20} \leq 26.3 \text{ b}$ the energy landscape does not change much when the size of the basis is increased. As we will see in Sec. IIIB, this range of quadrupole deformations is the one where the collective dynamics concentrates and, therefore, no significant differences are expected between the AMPGCM calculations with $M_{z,MAX}=14$ and $M_{z,MAX}=17$. Since the main interest of the present study is focussed on the two-neutron separation energies S_{2N} , rotational energy corrections, excitation energies, etc., and these quantities do not change very much with the considered $M_{z,MAX}$

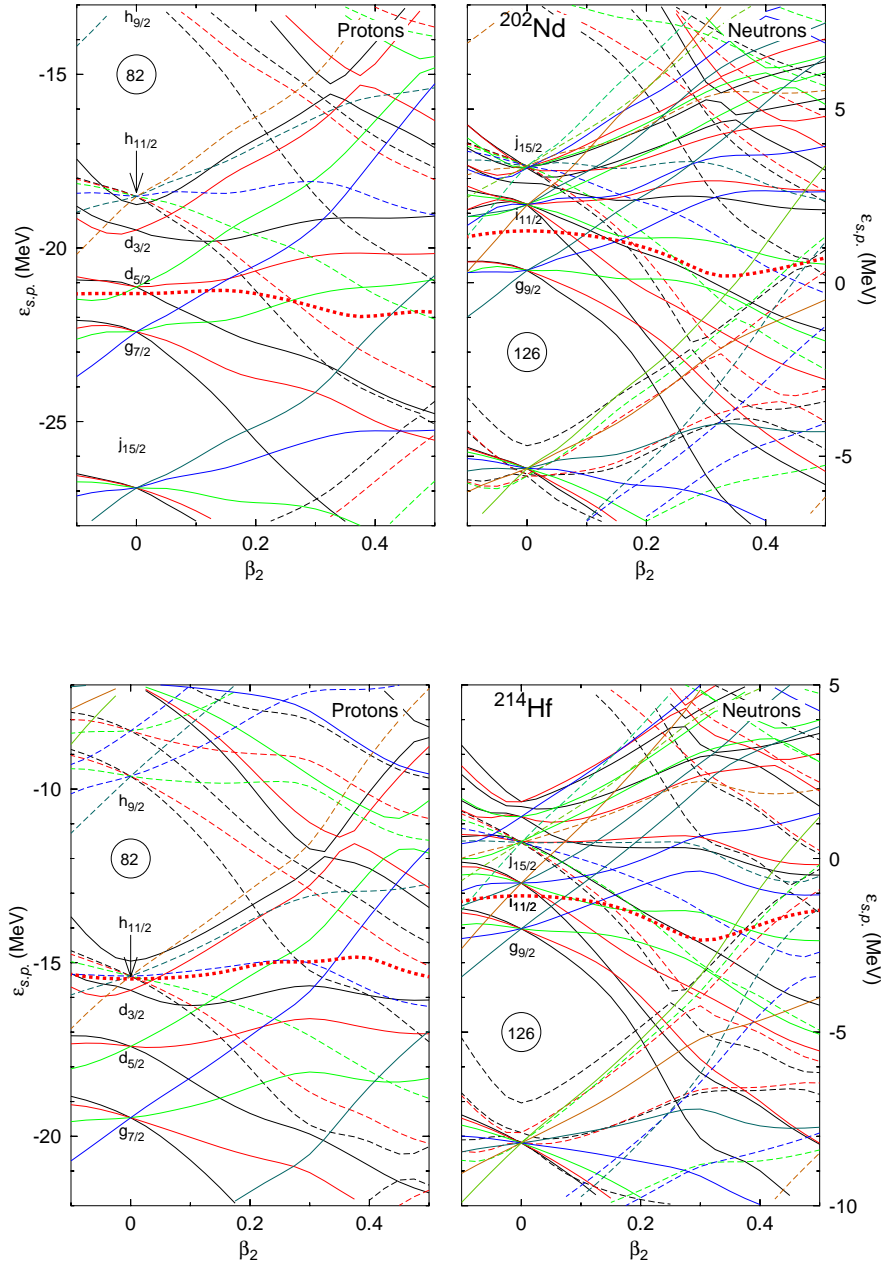


FIG. 7: (Color online) The proton and neutron SPEs, computed with the Gogny-D1M EDF, are plotted as a function of the β_2 deformation parameter for the $N=142$ nuclei ^{202}Nd and ^{214}Hf . Full (dashed) lines correspond to positive (negative) parity orbitals. Different K projections have associated a different color (black, red, green, blue, dark-green, brown, etc for $K = 1/2, 3/2, \dots$). The Fermi level is plotted with a thick red dashed line.

value, we conclude that $M_z, M_{ax}=14$ can be regarded as a reasonable compromise between accuracy and computational burden. To corroborate this conclusion, the two-neutron separation energies (full lines) computed within the HFB approximation are plotted in Fig. 5 as a function of neutron number. Results based on the Gogny-D1M EDF and the $M_z, M_{ax}=17$ and $M_z, M_{ax}=14$ bases

are shown in panels (a) and (b), respectively. The two-neutron separation energies obtained by restricting to spherical HFB calculations are also included in the plots (dashed lines) for comparison. One sees that the trends and numerical values predicted within the $M_z, M_{ax}=17$ and $M_z, M_{ax}=14$ calculations are quite similar, which corroborates our choice of $M_z, M_{ax}=14$ as a reasonable basis

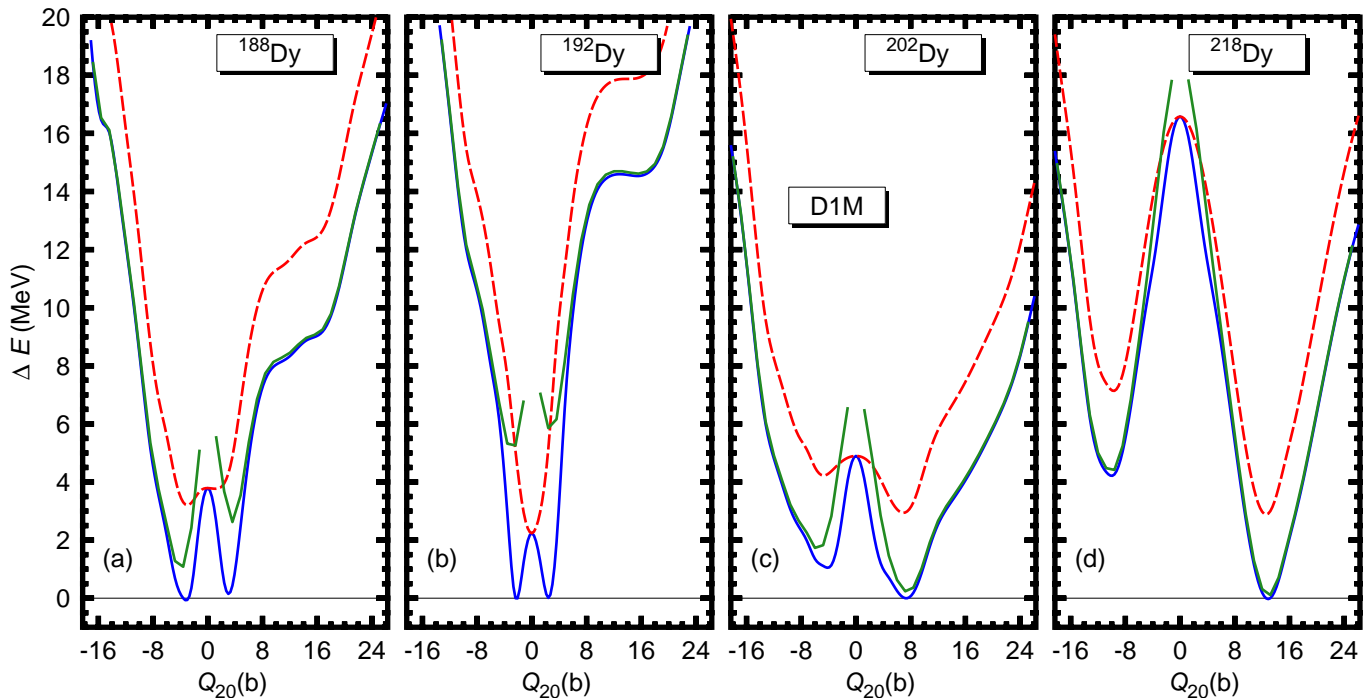


FIG. 8: (Color online) The AMPPECs for the nuclei $^{188,192,202,218}\text{Dy}$ and the spin values $I^\pi = 0^+$ (blue) and 2^+ (green) are depicted as a function of the quadrupole moment Q_{20} . The MFPECs (dashed red) are also included in the plots for comparison. All the energies are referred to the absolute minimum of the $I^\pi = 0^+$ AMPPECs. Results have been obtained with the parametrization D1M of the Gogny-EDF.

size to study the physical properties we are interested in this work.

The sudden decline in the S_{2N} values at $N=128$ is a manifestation of the strong $N=126$ shell closure. In going down from $Z=74$ (W) to $Z=60$ (Nd) no dramatic reduction occurs in the shell gap $\Delta_{shell} = S_{2N}(Z,126) - S_{2N}(Z,128)$ remaining strong enough as one approaches or even crosses the two-neutron dripline. This agrees well, with the strong shell effects predicted within the framework of the spherical RMF approximation [91].

As can be seen in Fig. 5, the two-neutron separation energies are well described in the framework of the spherical HFB approximation for $N=126, 128$ and 130 . However, the onset of slight oblate deformations at $N=122-124$ (see, Fig. 2) leads to S_{2N} values smaller than the ones obtained using the spherical HFB approximation. For all the considered isotopic chains, the difference with the spherical calculations becomes more dramatic beyond $N=132$. As we have discussed above, for such nuclei there is an onset of prolate ground state deformations (see, Fig. 2) that leads to an additional binding energy gain. As a result, an increase in the two-neutron separation energies takes place in going above $N=132$ with a ridge around the neutron number $N=140$. In general, two-neutron separation energies display a decline when adding further neutrons. Note that, while all the Nd isotopes remain unbound beyond $N=126$, the onset of prolate ground state deformations makes the nuclei $^{200,202,204}\text{Sm}$ stable against two-neutron decay. Furthermore, while in

the spherical HFB approach the two-neutron dripline is reached at $N=132$ and $N=140$ for the Gd and Dy isotopic chains, the presence of static ground state deformation effects in these chains shifts the location of the corresponding two-neutron driplines up to $N=148$ and $N=152$, respectively. For the remaining chains, the onset of ground state deformation enhances the stability with respect to the spherical HFB results in the neutron number range between $N=132$ and $N=156$.

The question that naturally arises is to what extent is this enhanced stability dependent on the particular Gogny-EDF employed at the HFB level. In Fig. 6, we show the two-neutron separation energies obtained with the Gogny-D1S EDF and $M_{z,Max}=14$. The observed trends resemble the ones already discussed for the Gogny-D1M EDF in Fig. 5. This is not surprising as both parametrizations provide similar HFB quadrupole deformation landscapes (see, Figs. 1 and 2). However, as already anticipated, the pronounced under-binding obtained with the Gogny-D1S EDF leads to systematically smaller S_{2N} values for increasing neutron number. Keeping this in mind, we conclude that the enhanced stability beyond the neutron shell closure $N=126$ is a genuine property of Gogny-like EDFs. This conclusion is further corroborated by resorting to the parametrization D1N [96] of the Gogny-EDF which provides S_{2N} values closer to the ones obtained with the D1M parameter set. Note that the results suggest, at least for some of the considered isotopic chains, a shift of the r-process path to

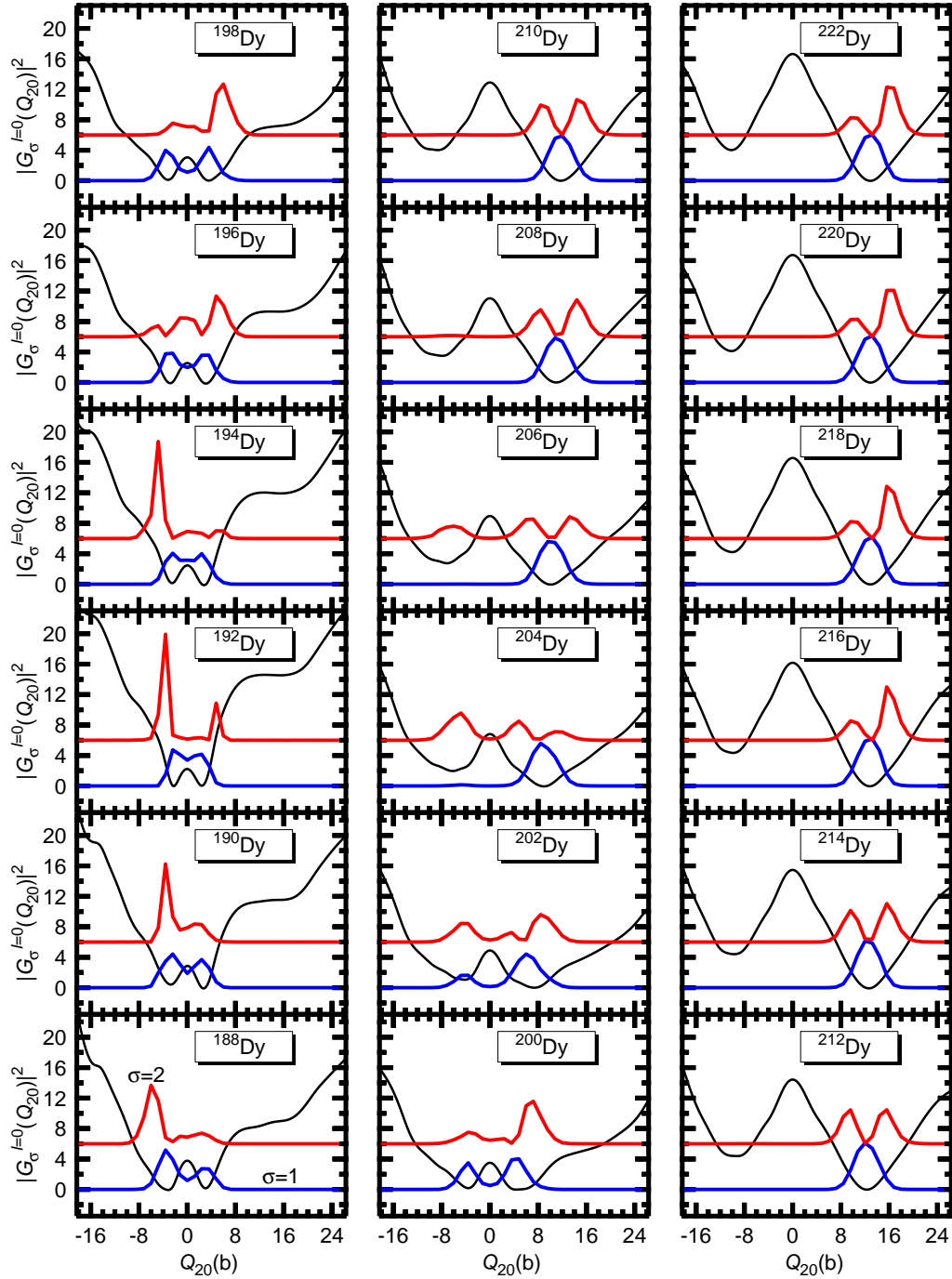


FIG. 9: (Color online) The square of the $I^\pi=0^+$ collective wave functions [Eq.(7)] corresponding to the ground ($\sigma=1$) and first excited ($\sigma=2$) states in the nuclei $^{188-222}\text{Dy}$ are plotted as a function of the quadrupole moment Q_{20} . The quantities actually depicted are $25 \times |G_{\sigma=1}^{I=0}(Q_{20})|^2$ (blue) and $6 + 25 \times |G_{\sigma=2}^{I=0}(Q_{20})|^2$ (red). For each nucleus the $I^\pi=0^+$ AMPPECs (black) are also included in the plots. Energies are always referred to the absolute minima of the corresponding AMPPECs. Results have been obtained with the parametrization D1M of the Gogny-EDF.

higher neutron numbers.

Having checked the robustness of the HFB predictions with respect to the considered parametrization of the Gogny-EDF, it is important to check their stability against quantum corrections stemming from the restoration of broken symmetries (mainly the rotational symme-

try) and quadrupole configuration mixing. In addition to ground state properties, such beyond mean field calculations also give access to excited states as well as other (dynamical) quadrupole properties in the studied nuclei.

Regardless of the Gogny-EDF employed one observes that in the Nd, Sm, Gd, Dy, Er, Yb, Hf and W chains the

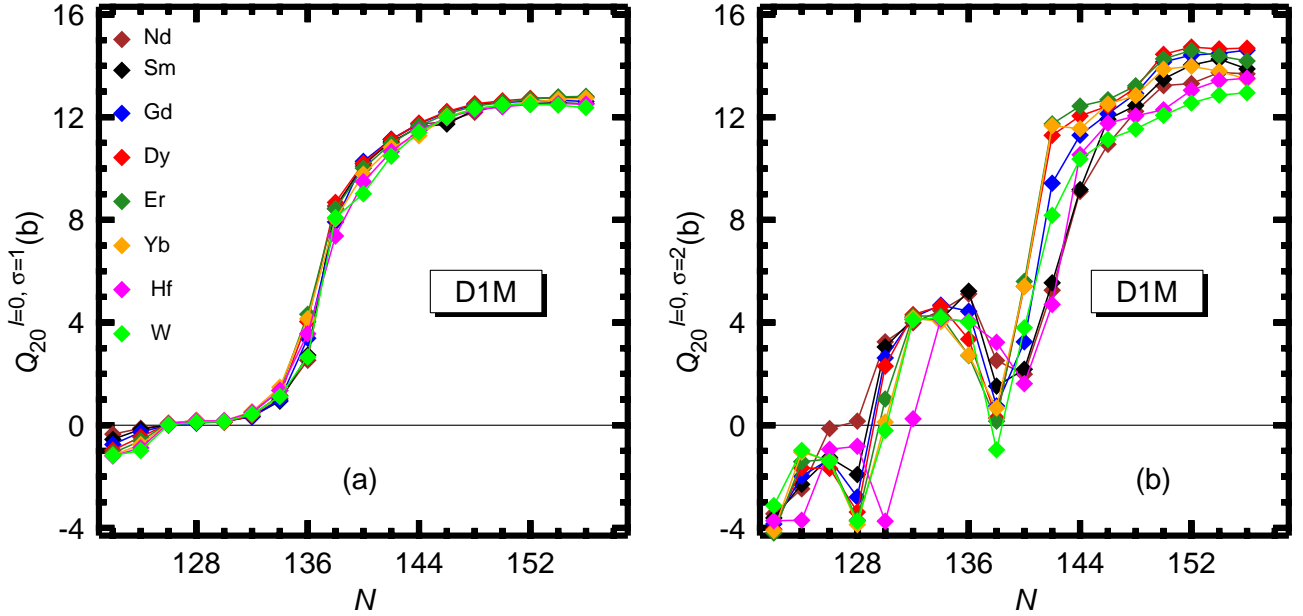


FIG. 10: (Color online) The intrinsic deformations [Eq.(8)] associated with the ground ($\sigma=1$) and first excited ($\sigma=2$) states at $I^\pi=0^+$ in the nuclei $^{182-216}\text{Nd}$, $^{184-218}\text{Sm}$, $^{186-220}\text{Gd}$, $^{188-222}\text{Dy}$, $^{190-224}\text{Er}$, $^{192-226}\text{Yb}$, $^{194-228}\text{Hf}$ and $^{196-230}\text{W}$ are depicted in panels (a) and (b), respectively, as a function of neutron number. Results have been obtained with the parametrization D1M of the Gogny-EDF. For more details, see the main text.

MFPECs become wider with increasing neutron number and display oblate local minima. For example, we have found (see, Fig. 1) that for $^{194-200}\text{Sm}$ these oblate local minima lie less than 2 MeV above the corresponding ground state. Such a shape coexistence also calls for a symmetry-projected configuration mixing analysis. For larger neutron numbers, the excitation energy of the oblate wells increases reaching its largest value (2.77 MeV and 3.87 MeV for the Gogny-D1S and Gogny-D1M EDFs, respectively) for ^{210}Sm . This comes along with the development of spherical barriers whose height reaches 10.72 MeV (12.26 MeV) in ^{218}Sm with the parametrization D1S (D1M). We stress, however, that even for those nuclei with well defined prolate wells it is important to carry out symmetry-projected configuration mixing calculations since the collective dynamics is determined not only by the energy landscape but also by the underlying inertia. With this in mind Gogny-D1M AMPGCM calculations have been carried out (see, Sec. III B) for all the nuclei studied in this paper.

Before ending this section, let us turn our attention to the evolution of the SPEs in the considered nuclei as a function of the deformation parameter β_2 . In Fig. 7 the proton and neutron SPEs, computed with the D1M parametrization, are depicted for the $N=142$ nuclei ^{202}Nd and ^{212}Hf . Both nuclei have a prolate deformed ground state minimum at $\beta_2 \approx 0.3$. The first noticeable fact is that both sets of SPEs look rather similar (up to global energy shifts) for both nuclei in spite of the 12 units difference in proton number. This result shows that the gross SPE behavior with deformation depends only on

the intrinsic shape of the nucleus and not on its proton and neutron number. It is just the position of the Fermi level that determines the deformation properties of the specific nucleus. In both nuclei we observe how the level density around $\beta_2 = 0.3$ decreases as compared with the neighboring regions signaling the existence of the ground state minimum at that deformation (Jahn-Teller effect). We also observe down-sloping neutron $j_{15/2}$ orbitals plunging in the Fermi sea and up-sloping neutron $g_{9/2}$ ones coming out. In the proton case, the down and up-sloping orbitals are different for ^{202}Nd and ^{214}Hf . We have down-sloping proton $h_{11/2}$ in the ^{202}Nd case and $h_{9/2}$ (coming from across the $Z=82$ shell closure) in the ^{214}Hf nucleus. In the former nucleus the $g_{7/2}$ is the predominant up-sloping orbital whereas in the later it is a combination of the $g_{7/2}$ (the $K = 7/2$ component) and the $d_{5/2}$.

B. The AMPGCM approximation: dynamical quadrupole properties

Before turning the attention to the AMPGCM, it is illustrative to analyze the behavior of the AMP energies as a function of the intrinsic quadrupole moment. In panels (a)-(d) of Fig. 8, the $I^\pi = 0^+$ and 2^+ AMPPECs are shown for the nuclei $^{188,192,202,218}\text{Dy}$ as a function of the quadrupole moment Q_{20} . The MFPECs have also been included in the plots for comparison. All the energies are referred to the absolute minimum of the $I^\pi = 0^+$ AMPPECs. The points omitted in the $I^\pi = 2^+$

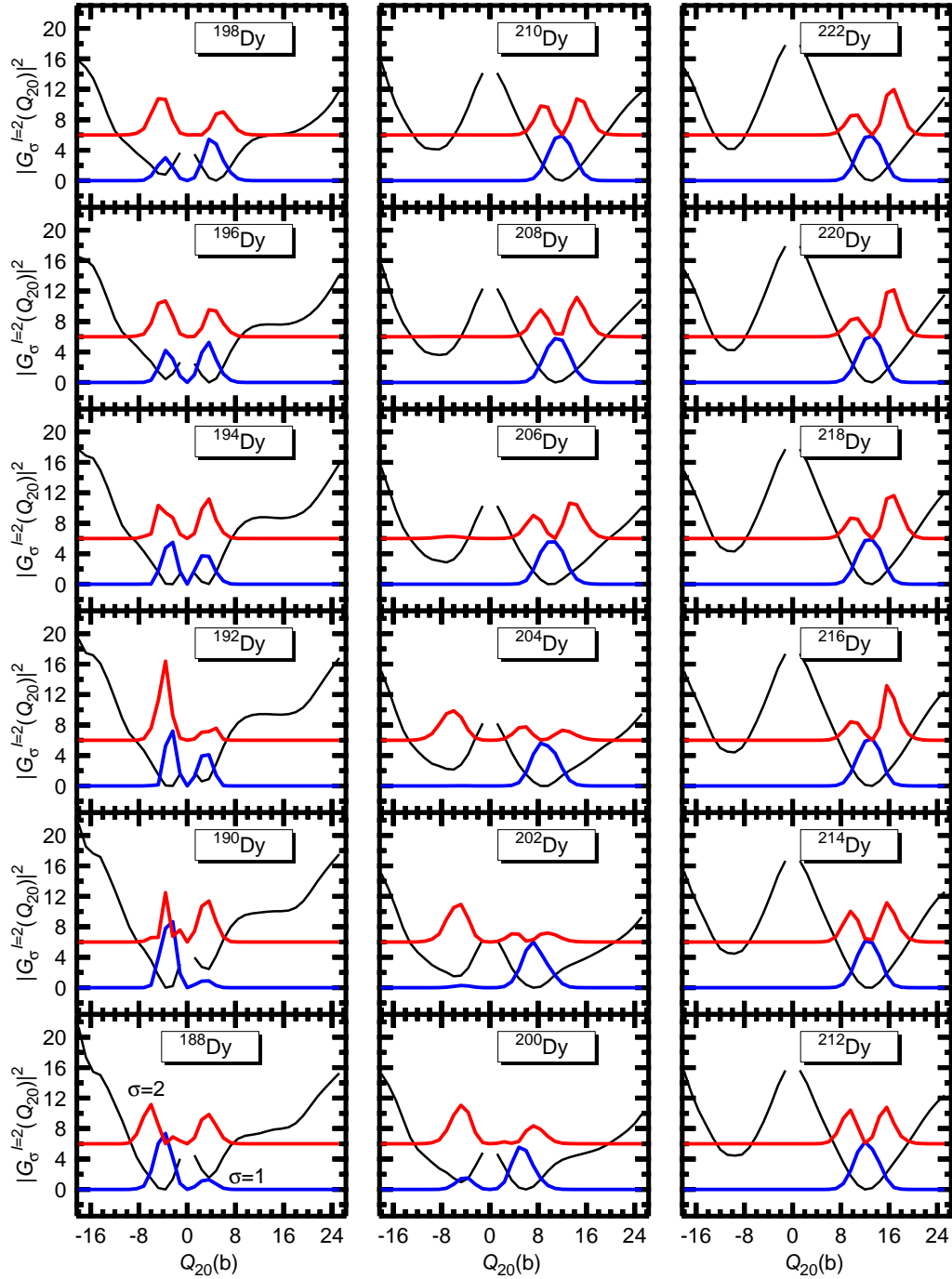


FIG. 11: (Color online) The square of the $I^\pi=2^+$ collective wave functions [Eq.(7)] corresponding to the ground ($\sigma=1$) and first excited ($\sigma=2$) states in the nuclei $^{188-222}\text{Dy}$ are plotted as a function of the quadrupole moment Q_{20} . The quantities actually depicted are $25 \times |G_{\sigma=1}^{I=2}(Q_{20})|^2$ (blue) and $6 + 25 \times |G_{\sigma=2}^{I=2}(Q_{20})|^2$ (red). For each nucleus the $I^\pi=2^+$ AMPPECs (black) are also included in the plots. Energies are always referred to the absolute minima of the corresponding AMPPECs. Results have been obtained with the parametrization D1M of the Gogny-EDF.

AMPPECs around $Q_{20}=0$ correspond to intrinsic configurations with a very small value of the norm overlap $\mathcal{N}^I(Q_{20}, Q_{20})$ [see, Eq.(5)] and can, therefore, be safely omitted since they do not play a role in the AMPGCM calculations to be discussed later on [11]. No energy gain is obtained due to AMP for the spherical configurations

and $I^\pi = 0^+$ since these are already pure 0^+ states with $\mathcal{N}^I(0, 0)=1$ [11, 13, 20, 32].

The comparison between the $I^\pi = 0^+$ AMPPECs and the MFPECs in both $^{188,192}\text{Dy}$ reveals the pronounced changes induced on the mean field energy landscapes due to the restoration of the broken rotational symmetry. In

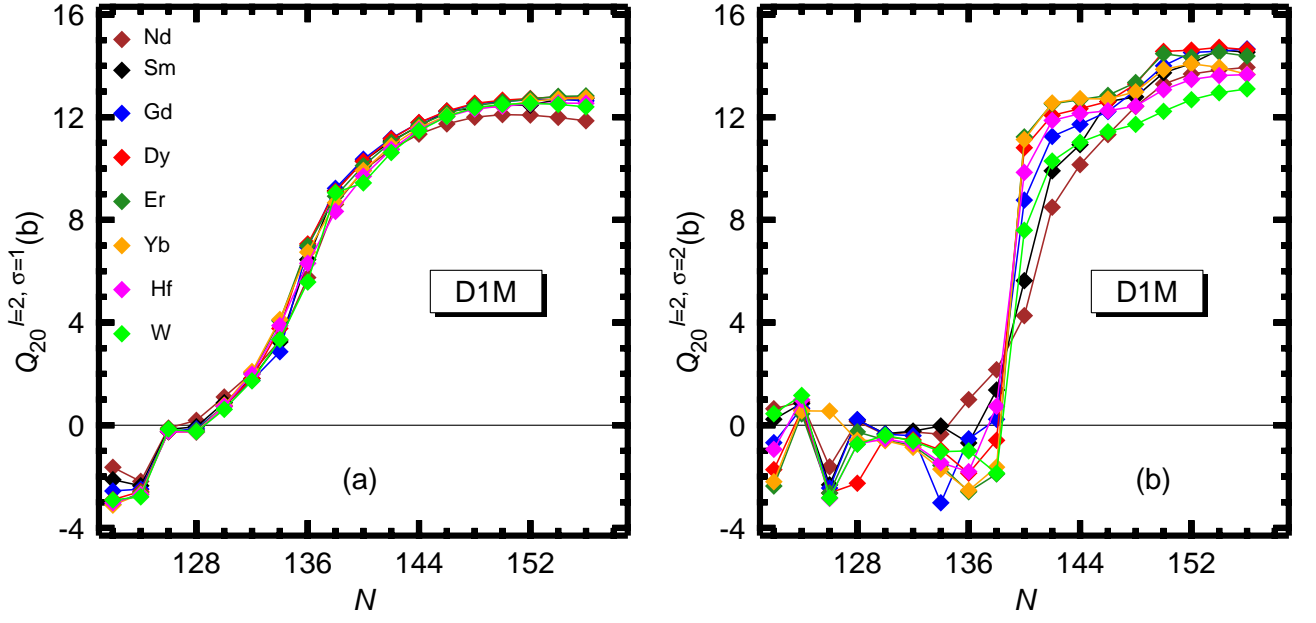


FIG. 12: (Color online) The intrinsic deformations [Eq.(8)] associated with the ground ($\sigma=1$) and first excited ($\sigma=2$) states at $I^\pi=2^+$ in the nuclei $^{182-216}\text{Nd}$, $^{184-218}\text{Sm}$, $^{186-220}\text{Gd}$, $^{188-222}\text{Dy}$, $^{190-224}\text{Er}$, $^{192-226}\text{Yb}$, $^{194-228}\text{Hf}$ and $^{196-230}\text{W}$ are depicted in panels (a) and (b), respectively, as a function of neutron number. Results have been obtained with the parametrization D1M of the Gogny-EDF. For more details, see the main text.

the case of ^{188}Dy , the 0^+ ground state corresponds to an oblate configuration with $Q_{20}=-3.6$ b while a low-lying prolate minimum ($\Delta E = 430$ keV) is found at $Q_{20}=3.6$ b. These minima are separated by a spherical barrier whose height is 3.79 MeV. While at the HFB level the ground state of the $N=126$ nucleus ^{192}Dy is spherical, once AMP is carried out two degenerate minima appear located at $Q_{20} = \pm 2.4$ b and separated by a barrier of 2.24 MeV. Such Q_{20} -symmetric degenerate minima have also been found for nuclei with spherical HFB ground states in several regions of the nuclear chart (see, for example, [11, 20, 32–34]) and their origin can be traced back to the behavior of the rotational energy correction [97] near sphericity. As we will see later in the framework of the AMPGCM scheme, the ground state collective wave function takes similar values around these two minima in such a way that the correlated ground state for ^{192}Dy is spherical. This seems to be a general feature as the same happens for all the other $N=126$ nuclei studied in this work. For the nuclei ^{202}Dy and ^{218}Dy , the 0^+ AMPPECs exhibit well pronounced prolate minima at $Q_{20}=7.2$ b and 13.2 b while the oblate ones are located at $Q_{20}=-4.8$ b and -9.6 b. The heights of the spherical barriers are 4.89 MeV and 16.58 MeV, respectively. In the case of the 2^+ AMPPECs, the absolute minima are oblate (prolate) deformed for the nuclei ^{188}Dy and ^{192}Dy (^{202}Dy and ^{218}Dy). Note, that the large excitation energy of 5.26 MeV for the oblate 2^+ minimum ($Q_{20}=-2.4$ b) in ^{192}Dy is consistent with the expectations for a spherical nucleus. The corresponding excitation energies for ^{202}Dy and ^{218}Dy decrease to 240 keV and 105 keV,

respectively. The plots in panels (a)-(d) of Fig. 8 already illustrate that a symmetry-projected configuration mixing analysis is required for the studied nuclei.

The square of the $I^\pi=0^+$ collective wave functions [Eq.(7)] corresponding to the ground ($\sigma=1$) and first excited ($\sigma=2$) states in the nuclei $^{188-222}\text{Dy}$ are plotted in Fig. 9 as a function of the quadrupole moment Q_{20} . To facilitate the reading of the plot, these quantities have been stretched and shifted according to the formulas $25 \times |G_{\sigma=1}^{I=0}(Q_{20})|^2$ and $6 + 25 \times |G_{\sigma=2}^{I=0}(Q_{20})|^2$. For each nucleus the AMPPECs are also included in the plots to guide the eye.

The 0_1^+ collective wave functions for the isotopes $^{188-200}\text{Dy}$ exhibit a significant admixture between the prolate and oblate minima found in the AMPPECs. In the case of the $N=126$ nucleus ^{192}Dy , the prolate and oblate configurations have practically the same weight and therefore its ground state turns out to be spherical on the average. The deformation effects found in the corresponding AMPPEC (see, Fig. 8) are not stable once quadrupole fluctuations are taken into account and $N=126$ remains, on the average (i.e., dynamically), as a spherical magic number not only for the Dy but also for all the studied isotopic chains. On the other hand, for the nuclei $^{202-222}\text{Dy}$ the 0_1^+ collective wave functions are well inside the prolate wells.

Having the collective wave functions $|G_{\sigma=1}^{I=0}(Q_{20})|^2$ at hand, we have computed the average ground state deformations $Q_{20}^{I=0, \sigma=1}$ [Eq.(8)]. They are plotted in panel (a) of Fig. 10 as a function of neutron number. It is satisfying to observe that the main trend obtained within the

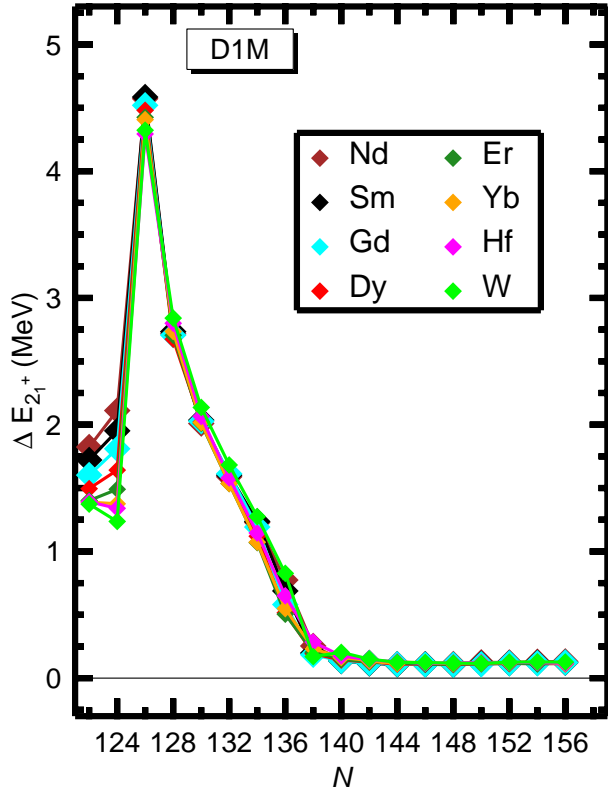


FIG. 13: (Color online) The excitation energies $\Delta E_{2_1^+} = E_{2_1^+} - E_{0_1^+}$ obtained in the framework of Gogny-D1M AMPGCM calculations are plotted as a function of neutron number.

HFB approximation [panel (a) of Fig. 2] does survive the effects of zero point quantum corrections, though the AMPGCM calculations provide smoother shape transitions than the mean field ones. For all the studied isotopic chains, the AMPGCM calculations predict the onset of (dynamical) prolate deformations for $N \geq 132$.

Coming back to Fig. 9, one sees that for the heavier Dy isotopes, the 0_2^+ collective wave functions display a behavior reminiscent of a β -vibrational band, i.e., they are located inside the prolate wells and have a node at a Q_{20} deformation where the 0_1^+ ground state wave functions attain their maximum value. The same pattern is also observed in the Nd, Sm, Gd, Er, Yb, Hf and W chains. However, at least in some nuclei, the 0_2^+ states are not symmetric around the node and, therefore, they cannot be considered as pure β -vibrations. The average deformations $Q_{20}^{I=0, \sigma=2}$ [Eq.(8)] corresponding to the 0_2^+ states have also been plotted in panel (b) of Fig.10. There is an onset of large prolate deformations in the 0_2^+ states around $N=140-142$. On the other hand, several shape transitions take place for $N \leq 138$. Though the overall trends are very similar, the precise location and nature of such shape transitions depend on the considered isotopic chain.

The square of the $I^\pi=2^+$ collective wave functions

for the ground ($\sigma=1$) and first excited ($\sigma=2$) states in $^{188-222}\text{Dy}$ is plotted in Fig. 11. For both $^{188,190}\text{Dy}$ the 2_1^+ states exhibit peaks on the oblate sector while for $^{192-198}\text{Dy}$ there is an admixture of prolate and oblate configurations in those states. On the other hand, for the neutron numbers $N \geq 134$ the 2_1^+ collective wave functions are well inside the prolate wells. The average deformations $Q_{20}^{I=2, \sigma=1}$ obtained for the Nd, Sm, Gd, Dy, Er, Yb, Hf and W chains are summarized in panel (a) of Fig. 12. In this case, the AMPGCM calculations predict a transition to prolate deformed 2_1^+ states for $N \geq 130$.

Coming back to Fig. 11, the 2_2^+ collective wave functions, as well as the ones obtained for other isotopic chains, display a transition to a quasi- β vibrational regime around the neutron number $N=140$. The corresponding $Q_{20}^{I=2, \sigma=2}$ values have been plotted in panel (b) of Fig. 12. Besides the shape transitions observed for lighter nuclei, there is an onset of large prolate deformations in the 2_2^+ states around $N=140-142$. The previous results indicate that, for all the studied nuclei, the AMPGCM zero point quantum corrections lead to predominant dynamical prolate deformations in the 0_1^+ , 0_2^+ , 2_1^+ and 2_2^+ states with increasing neutron number.

The excitation energies of the 2_1^+ states are plotted in Fig. 13 as a function of neutron number. The first noticeable feature is the pronounced peak at the neutron shell closure $N=126$. On the other hand, the decrease of the excitation energies observed for $N \geq 132$ is well correlated with the onset of prolate deformations found for both the 0_1^+ and 2_1^+ states in the AMPGCM calculations. Moreover, the values of such excitation energies remain small ($\Delta E_{2_1^+} < 300$ keV) and almost constant for nuclei with neutron numbers $N \geq 140$. This is precisely the neutron sector for which large prolate deformations are stabilized by the AMPGCM zero point quantum corrections [see, panel (a) of Figs. 10 and 12].

In panel (a) of Fig. 14 we have plotted (thick continuous lines with diamonds) the S_{2N} values, computed using the energies corresponding to the 0_1^+ AMPGCM ground states, as a function of neutron number. The two-neutron separation energies obtained within the HFB framework (thin continuous lines) and the ones corresponding to spherical calculations (dashed lines) are also included in the plot for comparison. It is satisfying to observe that the trends in the AMPGCM S_{2N} values support the enhanced stability predicted at the HFB level with respect to the spherical calculations. In particular, the ridge predicted at the mean field level around $N=140$ does survive the effects of symmetry-projected configuration mixing. However, the comparison between the AMPGCM and the HFB S_{2N} energies also reveals that while in the latter an enhancement only takes place beyond $N=132$ in the former it already occurs two mass units before. In addition, for all the considered isotopic chains, the AMPGCM two-neutron separation energies at $N=126$ are significantly smaller than the HFB ones while the corresponding values at $N=128$ are almost identical. This, as can be seen from panel (b), leads to smaller AMPGCM shell gaps.

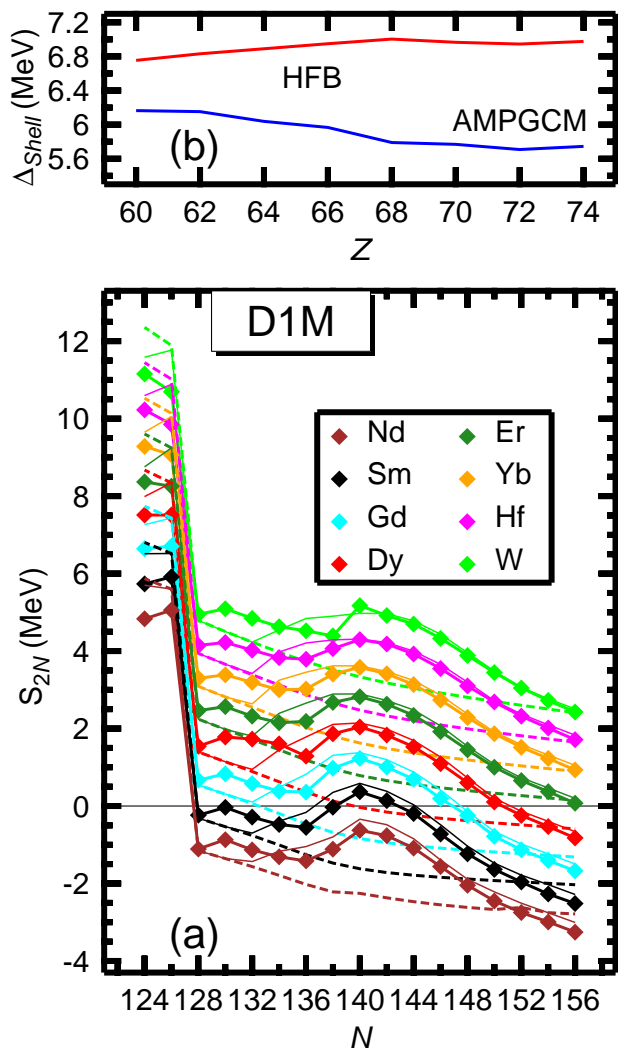


FIG. 14: (Color online) The S_{2N} values computed using the energies corresponding to the 0_1^+ AMPGCM ground states are depicted in panel (a) (thick continuous lines with diamonds) for the nuclei $^{182-216}\text{Nd}$, $^{184-218}\text{Sm}$, $^{186-220}\text{Gd}$, $^{188-222}\text{Dy}$, $^{190-224}\text{Er}$, $^{192-226}\text{Yb}$, $^{194-228}\text{Hf}$ and $^{196-230}\text{W}$ as a function of neutron number. The two-neutron separation energies obtained within the HFB framework (thin continuous lines) and the ones corresponding to spherical calculations (dashed lines) are also included in the plot for comparison. The AMPGCM (blue curve) and HFB (red curve) shell gaps are plotted in panel (b) as a function of proton number. All the results are obtained with the D1M parametrization. For more details, see the main text.

However we stress that, in spite of this dynamical reduction, the shell gap remains strong enough when moving down from $Z=74$ to $Z=60$. The quenched AMPGCM shell gap, as compared with the HFB one, and its smooth decrease with increasing Z values agree well with the results obtained for $N=126$ isotones in a previous (beyond mean field) global study of quadrupole correlation effects [98].

IV. CONCLUSIONS

In this work, we have considered the behavior of quadrupole collectivity across the $N=126$ neutron shell closure in the Nd, Sm, Gd, Dy, Er, Yb, Hf and W isotopic chains including very neutron-rich nuclei up to $N=156$. In the HFB framework $N=126$ nuclei are found to have spherical ground states and the corresponding mean field shell gaps do not exhibit a dramatic reduction when approaching or even crossing the two-neutron driplines.

Spherical HFB calculations are inappropriate to describe the static quadrupole properties of nuclei in the vicinity of the neutron shell closure. In particular, a shape transition to prolate deformed ground states is predicted to occur around $N=132-134$ within the (constrained) HFB framework. As a consequence of the onset of static axially symmetric quadrupole deformations there is an enhancement of the two-neutron separation energies that extends the corresponding two-neutron driplines far beyond what could be expected within spherical calculations. We have shown that such an enhanced stability is a genuine property of Gogny-like EDFs, i.e., it is independent of the particular parametrization employed in the calculations. The analysis of the SPEs reveals the presence of Jahn-Teller distortions in the corresponding proton and neutron spectra associated with the global and local minima found in the MFPECs.

Moreover, the constrained HFB calculations reveal that some nuclei display shape coexistence, i.e., low-lying prolate and oblate minima with similar energies. Such a shape coexistence also shows up in the AMPPECs and calls for a symmetry-projected configuration mixing analysis. Within this context, beyond mean field correlations, stemming from the restoration of the rotational symmetry broken at the HFB level and quadrupole fluctuations, have been taken into account, for all the considered Nd, Sm, Gd, Dy, Er, Yb, Hf and W nuclei, in the framework of the AMPGCM scheme based on the Gogny-D1M EDF.

Our AMPGCM calculations provide a dynamically correlated spherical ground state for all the studied $N=126$ nuclei. The AMPGCM correlations induce a reduction of the $N=126$ two-neutron shell gap as compared with the mean field one, in good agreement with other calculations [98]. However, we stress that on their own the AMPGCM shell gaps remain strong enough all the way down from $Z=74$ (W) to $Z=60$ (Nd).

Both the wave functions and average deformations obtained within the AMPGCM framework indicate that, with increasing neutron number, beyond mean field zero point quantum corrections stabilize dominant prolate configurations not only in the 0_1^+ but also in the 0_2^+ , 2_1^+ and 2_2^+ collective states. The dynamical onset of large deformations along the considered isotopic chains is well correlated, for example, with the behavior of the 2_1^+ excitation energies as a function of neutron number. On the other hand, for the heavier nuclei the 0_2^+ and 2_2^+ collective wave functions exhibit a behavior reminiscent of

β -vibrational bands.

It is found that, as a consequence of the onset of dynamical quadrupole deformations in the 0_1^+ states, the computed AMPGCM two-neutron separation energies corroborate the enhanced stability predicted at the mean field level. In particular, we have shown that the sudden spur in the two neutron separation energies, with a ridge around $N=140$, does survive the effects of zero point quantum fluctuations. Within this context, at least for some of the studied isotopic chains, the AMPGCM correlations shift the occurrence of the two-neutron driplines to higher neutron numbers.

We believe that the results discussed in this work deserve further attention not only from the nuclear structure side but also due to their possible consequences for the r-process path around $N=126$. A long list of task remains to be undertaken. For example, we have shown the independence of our HFB predictions with respect to

the Gogny-EDF employed in the calculations. It would be interesting to compare with the mean field and beyond mean field predictions arising from other state-of-the-art relativistic and nonrelativistic approaches. On the other hand, a more realistic treatment of pairing correlations, including a symmetry-projected analysis of the coupling between pairing and quadrupole degrees of freedom, is left for a future study. Work along these lines is in progress and will be published elsewhere.

Acknowledgments

The work of L. M. Robledo has been supported in part by the Spanish MINECO Grants No. FPA2012-34694, and No. FIS2012-34479 and by the Consolider-Ingenio 2010 Program MULTIDARK CSD2009-00064.

-
- [1] O. Sorlin and M. -G. Porquet, Prog. Part. Phys. **61**, 602 (2008).
- [2] S. Michimasa et al., Phys. Rev. C **89**, 054307 (2014).
- [3] C. Thibault et al., Phys. Rev. C **12**, 644 (1975).
- [4] T. Motobayashi et al., Phys. Lett. B **346**, 9 (1995).
- [5] C. Détraz et al., Phys. Rev. C **19**, 164 (1979).
- [6] D. Guillemaud-Mueller et al., Nucl. Phys. A **426**, 37 (1984).
- [7] B. Bastin et al., Phys. Rev. Lett. **99**, 022503 (2007).
- [8] S. Takeuchi et al., Phys. Rev. Lett. **109**, 182501 (2012).
- [9] E. Caurier, F. Nowacki, A. Poves and J. Retamosa, Phys. Rev. C **58**, 2033 (1998).
- [10] Y. Utsuno, T. Otsuka, T. Mizusaki and M. Honma, Phys. Rev. C **60**, 054315 (1999).
- [11] R. Rodríguez-Guzmán, J.L. Egido and L.M. Robledo Nucl. Phys. A **709**, 201 (2002).
- [12] R. Rodríguez-Guzmán, J.L. Egido and L.M. Robledo, Phys. Lett. B **474**, 15 (2000).
- [13] R. Rodríguez-Guzmán, J.L. Egido and L.M. Robledo, Phys. Rev. C **62**, 054319 (2000).
- [14] R. Rodríguez-Guzmán, J.L. Egido and L.M. Robledo, Eur. Phys. J. A **17**, 37 (2003).
- [15] S. Péru, M. Girod and J. F. Berger, Eur. Phys. J. A **9**, 35 (2000).
- [16] G. A. Lalazissis, A. R. Farhan and M. M. Sharma, Nucl. Phys. A **628**, 221 (1998).
- [17] J. Terasaki, H. Flocard, P. -H. Heenen and P. Bonche, Nucl. Phys. A **621**, 706 (1997).
- [18] M. V. Stoisov, J. Dobaczewski, P. Ring and S. Pittel, Phys. Rev. C **61**, 034311 (2000).
- [19] J. Retamosa, E. Caurier, F. Nowacki and A. Poves, Phys. Rev. C **65**, 1266 (1997).
- [20] R. Rodríguez-Guzmán, J.L. Egido and L.M. Robledo, Phys. Rev. C **65**, 024304 (2002).
- [21] T. R. Werner, J. A. Sheikh, W. Nazarewicz, M. R. Strayer, A. S. Umar and M. Misu, Phys. Lett. B **335**, 259 (1994).
- [22] D. Hirata, K. Sumiyoshi, B. V. Carlson, H. Toki and I. Tanihata, Nucl. Phys. A **609**, 131 (1996).
- [23] G. A. Lalazissis, D. Vretenar, P. Ring, M. Stoisov and L. M. Robledo, Phys. Rev. C **60**, 014310 (1999).
- [24] M. Lewitowicz et al., Nucl. Phys. A **496**, 477 (1989).
- [25] O. Sorlin et al., Phys. Rev. C **47**, 2941 (1993).
- [26] H. Scheit et al., Phys. Rev. Lett. **77**, 3967 (1996).
- [27] T. Glasmacher et al., Phys. Lett. B **395**, 163 (1997).
- [28] P. Ring and P. Schuck, *The Nuclear Many-Body Problem* (Springer, Berlin, 1980).
- [29] S. Péru and M. Martini, Eur. Phys. J. A **50**, 88 (2014).
- [30] T. Nitsić, D. Vretenar and P. Ring, Phys. Rev. C **73**, 034308 (2006).
- [31] T. Nitsić, D. Vretenar and P. Ring, Phys. Rev. C **74**, 064309 (2006).
- [32] R. R. Rodríguez-Guzmán, J. L. Egido and L. M. Robledo, Phys. Rev. C **69**, 054319 (2004).
- [33] T. Duguet, M. Bender, P. Bonche and P. -H. Heenen, Phys. Lett. B **559**, 201 (2003).
- [34] M. Bender, P. Bonche, T. Duguet, P. -H. Heenen, Phys. Rev. C **69**, 064303 (2004).
- [35] B. Pfeiffer, K. L. Kratz, F. K. Thielemann and W. B. Walters, Nucl. Phys. A **693**, 282 (2001).
- [36] K. L. Kratz, J. P. Bitouzet, F. K. Thielemann, P. Möller and B. Pfeiffer, Astrophys. J. **403**, 216 (1993).
- [37] M. Arnould, S. Goriely and K. Takahashi, Phys. Rep. **450**, 97 (2007).
- [38] E. M. Burbidge, G. R. Burbidge, A. A. Fowler and F. Hoyle, Rev. Mod. Phys. **29**, 547 (1957).
- [39] S. Wanajo, S. Goriely, M. Samyn and N. Itoh, Astrophys. J. **606**, 1057 (2004).
- [40] J. Dobaczewski, I. Hamamoto, W. Nazarewicz and J. A. Sheikh, Phys. Rev. Lett. **72**, 981 (1994).
- [41] B. Chen, J. Dobaczewski, K. L. Kratz, K. Langanke, B. Pfeiffer, F. -K. Thielemann and P. Vogel, Phys. Lett. B **355**, 37 (1995).
- [42] M. M. Sharma, G. A. Lalazissis, W. Hillebrandt and P. Ring, Phys. Rev. Lett. **72**, 1431 (1994).
- [43] M. M. Sharma, G. A. Lalazissis, W. Hillebrandt and P. Ring, Phys. Rev. Lett. **73**, 1870 (1994).
- [44] M. M. Sharma and A. R. Farhan, Phys. Rev. C **65**, 044301 (2002).
- [45] B. Pfeiffer, K. L. Kratz, F. K. Thielemann and W. B.

- Walters, Z. Phys. A **357**, 235 (1997).
- [46] J. M. Pearson, R. C. Nayak and S. Goriely, Phys. Lett. B **387**, 455 (1996).
- [47] I. Dillmann, K. -L. Kratz, A. Wöhr, O. Arndt, B. A. Brown, P. Hoff, M. Hjorth-Jensen, U. Köster, A. N. Ostrowski, B. Pfeiffer, D. Seweryniak, J. Shergur, W. B. Walters and the ISOLDE Collaboration, Phys. Rev. Lett. **91**, 162503 (2003).
- [48] T. R. Rodríguez, J. L. Egido and A. Jungclaus, Phys. Lett. B **668**, 410 (2008).
- [49] A. Jungclaus, L. Cáceres, M. Górska, M. Pfützner, S. Pietri, E. Werner-Malento, H. Grawe, K. Langanke, G. Martínez-Pinedo, F. Nowacki, J. J. Cuenca-García, D. Rudolph, Z. Podolyák, P. H. Reagan, P. Detistov, S. Lalkovski, V. Modamio, J. Walker, P. Bednarczyk, P. Doornenbal, H. Geissel, J. Gerl, J. Grebosz, I. Kojouharov, N. Kurz, W. Prokopowicz, H. Schaffner, H. J. Wollersheim, K. Andgren, J. Benlliure, G. Benzoni, A. M. Bruce, E. Casajeros, B. Cederwall, F. C. L. Crespi, B. Hadinia, M. Hellström, R. Hoischen, G. Ilie, J. Jolie, A. Khaplanov, M. Kmiecik, R. Kumar, A. Maj, S. Mandal, F. Montes, S. Myalski, G. S. Simpson, S. J. Steer, S. Tashenov and O. Wieland, Phys. Rev. Lett. **99**, 132501 (2007).
- [50] M. Górska, L. Cáceres, H. Grawe, M. Pfützner, A. Jungclaus, E. Werner-Malento, Z. Podolyák, P. H. Reagan, D. Rudolph, P. Detistov, S. Lalkovski, V. Modamio, J. Walker, T. Beck, P. Bednarczyk, P. Doornenbal, H. Geissel, J. Gerl, J. Grebosz, R. Hoischen, I. Kojouharov, N. Kurz, W. Prokopowicz, H. Schaffner, H. Weick, H. J. Wollersheim, K. Andgren, J. Benlliure, G. Benzoni, A. M. Bruce, E. Casajeros, B. Cederwall, F. C. L. Crespi, B. Hadinia, M. Hellström, G. Ilie, A. Khaplanov, M. Kmiecik, R. Kumar, A. Maj, S. Mandal, F. Montes, S. Myalski, G. S. Simpson, S. J. Steer, S. Tashenov, Zs. Dombrádi, R. Reiter and D. Sohler, Phys. Lett. B **672**, 313 (2009).
- [51] S. Goriely, S. Hilaire, M. Girod and S. Péru, Phys. Rev. Lett. **102**, 242501 (2009).
- [52] J. Dechargé and D. Gogny, Phys. Rev. C **21**, 1568 (1980)
- [53] J. F. Berger, M. Girod, and D. Gogny, Nucl. Phys. A **428**, 23c (1984).
- [54] J. L. Egido, L. M. Robledo and R. R. Rodríguez-Guzmán, Phys. Rev. Lett. **93** 082502 (2004).
- [55] R. Rodríguez-Guzmán, L.M. Robledo and P. Sarriguren, Phys. Rev. C **86**, 034336 (2012).
- [56] R. Rodríguez-Guzmán, L.M. Robledo, P. Sarriguren and J. E. García-Ramos, Phys. Rev. C **81**, 024310 (2010).
- [57] J. -P. Delaroche, M. Girod, H. Goutte and J. Libert, Nucl. Phys. A **771**, 103 (2006).
- [58] G. F. Berstch, M. Girod, S. Hilaire, J. -P. Delaroche, H. Goutte and S. Péru, Phys. Rev. Lett. **99**, 032502 (2007).
- [59] J. -P. Delaroche, M. Girod, J. Libert, H. Goutte, S. Hilaire, S. Péru, N. Pillet and G. F. Berstch, Phys. Rev. C **81**, 014303 (2010).
- [60] S. Hilaire and M. Girod, Eur. Phys. J. A **33**, 237 (2007).
- [61] T. R. Rodríguez, A. Arzhanov and G. Martínez-Pinedo, arXiv/nucl-th/1407.7699 (2014).
- [62] R. Rodríguez-Guzmán and L.M. Robledo, Phys. Rev. C **89**, 054310 (2014).
- [63] R. Rodríguez-Guzmán and L.M. Robledo, Eur. Phys. J. **A50**, 142 (2014).
- [64] R. Rodríguez-Guzmán, P. Sarriguren, L. M. Robledo and S. Perez-Martin, Phys. Lett. B **691**, 202 (2010).
- [65] R. Rodríguez-Guzmán, P. Sarriguren and L. M. Robledo, Phys. Rev. C **82**, 061302(R) (2010).
- [66] R. Rodríguez-Guzmán, P. Sarriguren and L. M. Robledo, Phys. Rev. C **83**, 044307 (2011).
- [67] A. Valor, P. -H. Heenen, P. Bonche, Nucl. Phys. A **671**, 145 (2000).
- [68] P. Bonche, J. Dobaczewski, H. Flocard, P. -H. Heenen and J. Meyer, Nucl. Phys. A **510**, 466 (1990).
- [69] K. W. Schmid, F. Grümmer and A. Faessler, Phys. Rev. C **29**, 291 (1984).
- [70] K. W. Schmid, F. Grümmer and A. Faessler, Phys. Rev. C **29**, 308 (1984).
- [71] K. Hara, A. Hayashi and P. Ring, Nucl. Phys. A **385**, 14 (1982).
- [72] K. Hara and Y. Sun, Int. J. Mod. Phys. E **4**, 637 (1995).
- [73] L. M. Robledo, Phys. Rev. C **50**, 2874 (1994).
- [74] J. Dobaczewski, W. Nazarewicz, T. R. Werner, J. F. Berger, C. R. Chinn and J. Dechargé, Phys. Rev. C **53**, 2809 (1996).
- [75] J. Dobaczewski, H. Flocard and J. Treiner, Nucl. Phys. A **422**, 103 (1994).
- [76] L.M. Robledo and G. F. Berstch, Phys. Rev. C **84**, 014312 (2011).
- [77] L.M. Robledo and R. Rodríguez-Guzmán, J. Phys. G: Nucl. Part. Phys. **39**, 105103 (2012).
- [78] R. Rodríguez-Guzmán, C. A. Jiménez-Hoyos, R. Schutski and G. E. Scuseria, Phys. Rev. B **87**, 235129 (2013).
- [79] R. Rodríguez-Guzmán, C. A. Jiménez-Hoyos and G. E. Scuseria, Phys. Rev. B **89**, 195109 (2014).
- [80] C. A. Jiménez-Hoyos, R. Rodríguez-Guzmán and G. E. Scuseria, J. Chem. Phys. **139**, 224110 (2013).
- [81] C. A. Jiménez-Hoyos, R. Rodríguez-Guzmán and G. E. Scuseria, J. Chem. Phys. **139**, 204102 (2013).
- [82] P. A. Butler and W. Nazarewicz, Rev. Mod. Phys. **68**, 349 (1996).
- [83] L. M. Robledo, M. Baldo, P. Schuck and X. Vinas, Phys. Rev. C **81**, 034315 (2010).
- [84] L. M. Robledo, R. Rodríguez-Guzmán and P. Sarriguren, J. Phys. G: Nucl. Part. Phys. **36**, 115104 (2009).
- [85] A.R.Edmonds, *Angular Momentum in Quantum Mechanics*, Princeton Univ. Press, Princeton (1957).
- [86] D. L. Hill and J. A. Wheeler, Phys. Rev. **89**, 1102 (1953).
- [87] M. Bender, P. -H. Heenen and P. -G. Reinhard, Rev. Mod. Phys. **75**, 121 (2003).
- [88] M. Bender, G. F. Bertsch and P. -H. Heenen, Phys. Rev. Lett. **94**, 102503 (2005).
- [89] L. M. Robledo, Int. J. Mod. Phys. E **16**, 337 (2007).
- [90] J. L. Egido and L. M. Robledo, Nucl. Phys. A **524**, 65 (1991).
- [91] A. R. Farhan and M. M. Sharma, Phys. Rev. C **73**, 045803 (2006).
- [92] M. M. Sharma and A. A. Saldanha, Kuwait J. Sci. Engg. **38**, 39 (2011).
- [93] A. R. Farhan and M. M. Sharma, to be published.
- [94] S. Goriely, M. Samyn and J. M. Pearson, Phys. Rev. C **75**, 064312 (2007).
- [95] P. Möller, J. Nix and W. Swiatecki, At. Data Nucl. Data Tables **59**, 185 (1994).
- [96] F. Chappert, M. Girod, and S. Hilaire, Phys. Lett. B **668**, 420 (2008).
- [97] J.L Egido and L.M. Robledo, Lecture Notes in Physics **641**, 269 (2004).
- [98] M. Bender, G. F. Bertsch and P. -H. Heenen, Phys. Rev. C **73**, 034322 (2006).